nature materials

LETTERS

https://doi.org/10.1038/s41563-019-0506-1

Pressure-controlled interlayer magnetism in atomically thin CrI_3

Tingxin Li[1,6], Shengwei Jiang[2,6], Nikhil Sivadas[1], Zefang Wang[1], Yang Xu[1], Daniel Weber[3], Joshua E. Goldberger[3], Kenji Watanabe[4], Takashi Taniguchi[4], Craig J. Fennie[1], Kin Fai Mak[1,2,5]* and Jie Shan[1,2,5]*

Stacking order can influence the physical properties of two-dimensional van der Waals materials[1,2]. Here we applied hydrostatic pressure up to 2 GPa to modify the stacking order in the van der Waals magnetic insulator CrI_3. We observed an irreversible interlayer antiferromagnetic-to-ferromagnetic transition in atomically thin CrI_3 by magnetic circular dichroism and electron tunnelling measurements. The effect was accompanied by a monoclinic-to-rhombohedral stacking-order change characterized by polarized Raman spectroscopy. Before the structural change, the interlayer antiferromagnetic coupling energy can be tuned up by nearly 100% with pressure. Our experiment reveals the interlayer ferromagnetic ground state, which is established in bulk CrI_3 but not observed in native exfoliated thin films. The observed correlation between the magnetic ground state and the stacking order is in good agreement with first principles calculations[3–8] and suggests a route towards nanoscale magnetic textures by moiré engineering[3,9].

Intrinsic magnetism in two-dimensional (2D) van der Waals materials has received growing attention[10–14]. Of particular interest is the thickness-dependent magnetic ground state in atomically thin CrI_3. In these exfoliated thin films, the magnetic moments are aligned (in the out-of-plane direction) in each layer, but prefer to be anti-aligned in adjacent layers[8,14–24]. As a result, monolayer CrI_3 is a ferromagnet, CrI_3 bilayer is an antiferromagnet and thicker samples can contain a mixture. The relatively weak interlayer coupling compared to the intralayer coupling allows the effective control of the interlayer magnetism, which has led to interesting spintronics applications, including voltage switching[15–17], spin filtering[8,18–21] and spin transistors[22]. The origin of interlayer antiferromagnetic (AF) coupling is, however, not well understood as an interlayer ferromagnetic (FM) order is believed to be the ground state in bulk crystals. Recent ab initio calculations[3–8] and experiments[23,24] suggest that the stacking order could provide an explanation, but a direct correlation between stacking order and interlayer magnetism is lacking.

In bulk CrI_3, the Cr atoms in each layer form a honeycomb structure, and each Cr atom is surrounded by six I atoms in an octahedral coordination (Fig. 1a). The bulk crystals undergo a structural phase transition at around 210–220 K from a monoclinic phase (space group $C2/m$) to a rhombohedral phase (space group $R\bar{3}$) on cooling[25,26] with a small volume reduction. The major difference between the two phases is the stacking order, whereas the in-plane structure remains nearly unchanged. In the monoclinic phase, each layer is displaced by a translation vector of (1/3, 0), but in the rhombohedral phase by (1/3, −1/3) in the ABC order (Fig. 1a). The structural change can be characterized by polarized Raman spectroscopy (Methods gives details). Figure 1b shows the Raman spectra of a bulk CrI_3 crystal recorded at 300 K and at 90 K in the back-scattering crossed-polarization configuration. For the rhombohedral phase, the peak near $107\,\mathrm{cm}^{-1}$ is a twofold degenerate E_g mode, whose energy and intensity are independent of the polarization angle (right panel, Fig. 1c). In contrast, for the monoclinic phase with a lower symmetry, the mode splits into A_g and B_g modes with distinct selection rules[26–28], which give rise to one unresolved peak with a fourfold polarization dependence for the peak energy (left panel, Fig. 1c).

In this study, we applied hydrostatic pressure on exfoliated CrI_3 thin films of 2–9 layers to investigate the pressure effect on the material's magnetic properties. A similar study was reported independently by Song et al.[29]. The strong structural anisotropy means that the hydrostatic pressure on layered materials practically only modifies the interlayer structure, such as the layer separation and stacking order. For all the measurements, we used samples in the form of tunnel junctions with atomically thin CrI_3 as a barrier and few-layer graphene as the electrodes. The devices were encapsulated with hexagonal boron nitride (hBN) on both sides to protect CrI_3 from the environmental effect. A piston high-pressure cell compatible with electrical transport measurements was used to apply pressure up to 2 GPa. The pressure effect on the magnetic properties of CrI_3 was monitored by the tunnel magnetoresistance. Magnetic circular dichroism (MCD) microscopy and polarized Raman spectroscopy were employed to characterize the magnetic state and the crystal structure of CrI_3, respectively, before and after applying pressure. The MCD data were taken at 3.5 K and the tunnel conductance data at 1.7 K unless otherwise specified. As pressure can be varied only at room temperature, the samples typically went through many thermal cycles (under zero magnetic field) during the measurements. Methods gives details on the bulk crystal growth and device fabrication, as well as on the pressure cell and the MCD measurements.

Figure 2a is an optical micrograph of a device employed in this experiment and Fig. 2b is the side view of the device schematics. Figure 2c is the image of the CrI_3 barrier before it was integrated into the tunnel junction device. The film consists mostly of two-layer and five-layer regions. We applied pressure of 1.8 GPa on the tunnel junction at room temperature, cooled it down to 1.7 K with

---

[1]School of Applied and Engineering Physics, Cornell University, Ithaca, NY, USA. [2]Laboratory of Atomic and Solid State Physics, Cornell University, Ithaca, NY, USA. [3]Department of Chemistry and Biochemistry, The Ohio State University, Columbus, OH, USA. [4]National Institute for Materials Science, Tsukuba, Japan. [5]Kavli Institute at Cornell for Nanoscale Science, Ithaca, NY, USA. [6]These authors contributed equally: Tingxin Li, Shengwei Jiang. *e-mail: kinfai.mak@cornell.edu; jie.shan@cornell.edu

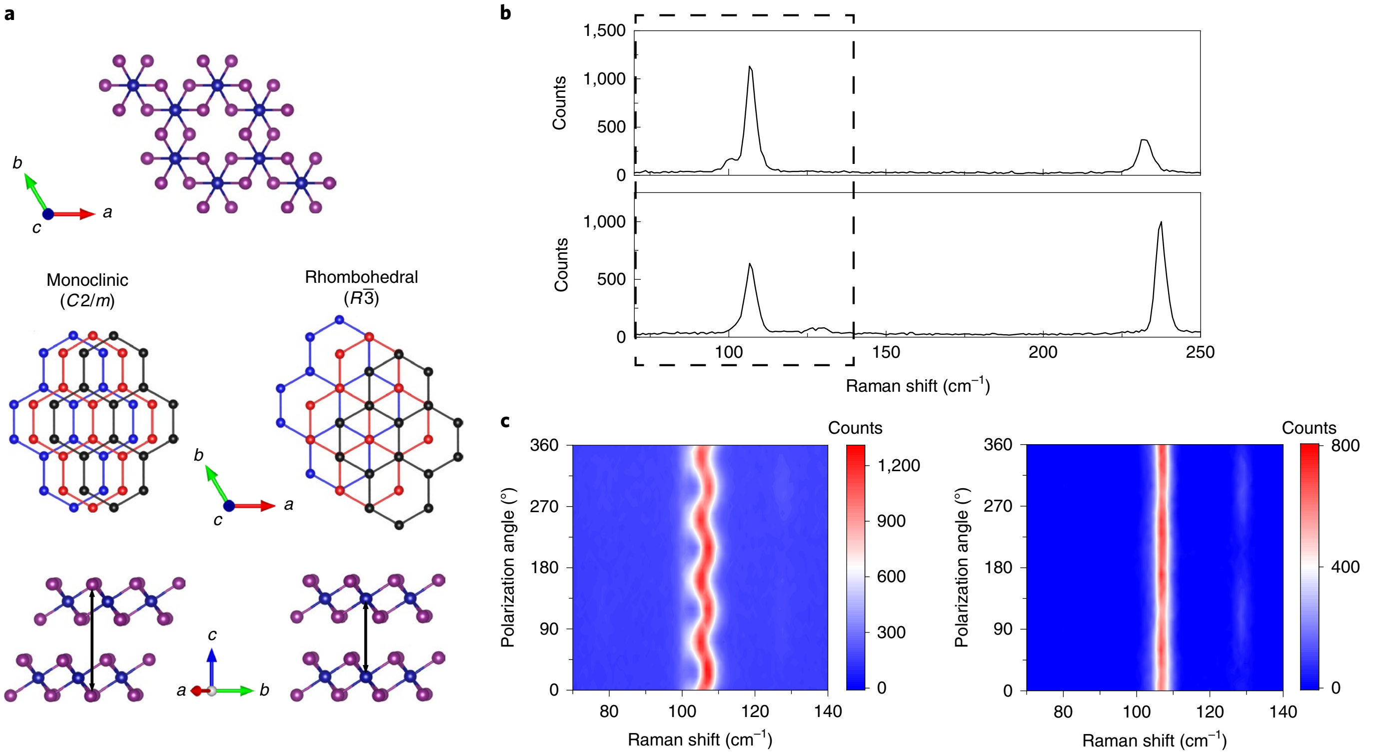

Fig. 1 | Crystal structure of CrI$_3$. a, Top: atomic structure of monolayer CrI$_3$. Cr atoms (blue balls) form a honeycomb lattice structure. Each Cr atom is surrounded by six I atoms (purple balls) in an octahedral coordination. Middle: top view of the stacking order in the monoclinic (left) and rhombohedral (right) phases for three layers. The Cr network shifts in the order of blue, red and black. Bottom: side view of the corresponding stacking order for two layers, and the alignment of atoms in the two layers along the *c* direction is indicated by the double-sided vertical black arrows. *a*, *b* and *c* are the crystallographic axes. **b**, Polarized Raman spectra of a bulk CrI$_3$ crystal at 300 K (upper) and 90 K (lower) in the crossed-polarization configuration. **c**, Polarization angle dependence of the spectrum inside the dashed box in **b**. The peak energy of the mode around 107 cm^{-1} shows a fourfold dependence on the polarization angle in the monoclinic phase (left), and no dependence in the rhombohedral phase (right).

pressure and released pressure after the sample was warmed back up to room temperature. Figure 2d shows the MCD image of the sample at 633 nm under a zero field before (left) and after (right) applying pressure. Accordingly, Fig. 2e shows the magnetic field dependence of MCD at selected locations. The MCD probes the sample magnetization, but its magnitude in samples of different thicknesses cannot be compared directly due to the variations in their spectral response and local field factor.

Before applying pressure, the MCD signal under zero field was nearly vanishing across the entire two-layer region and was finite (but generally weak) in the five-layer region. This is consistent with the interlayer AF order: two-layer CrI$_3$ is an antiferromagnet, and five-layer is a ferromagnet due to an uncompensated layer. This is further seen in Fig. 2e (left panel). In addition to the FM loop centred at zero field, both five-layer regions exhibited two spin-flip transitions: one near 0.75 T and the other near 1.7 T. These transitions correspond to the spin flips at the surface layers and at the interior layers of the sample, respectively. Above the second transition field, the magnetic moments in all the layers aligned. As interior layers were absent in bilayers, there was only one spin-flip transition near 0.75 T. At these transitions (first-order phase transitions), hysteresis was clearly visible (Fig. 2e). These observations are in good agreement with the reported results[14–19]. The MCD image also shows the presence of inhomogeneities. In particular, the non-vanishing signal in even-layer-number regions and the significantly higher signal in certain five-layer regions are probably from stacking faults, which can introduce interlayer FM coupling, as discussed below.

The results become dramatically different after applying pressure (right panel, Fig. 2d,e). A significantly higher MCD signal at zero field emerged almost everywhere, which potentially suggests an interlayer AF–FM phase transition in atomically thin CrI$_3$. This is supported by the magnetic field dependence of MCD in both five-layer regions and the two-layer region denoted by dots in Fig. 2c: a clear hysteresis loop centred at zero field was observed (Fig. 2e). The FM phase persisted to about 60 K in these regions (Fig. 2f), which agrees well with the Curie temperature of the bulk crystal. The MCD result also shows that the pressure-induced AF–FM phase transition is not complete in many locations across the sample. For instance, a mixed FM and AF response with a visible spin-flip transition is observed over a probe area of about 1 μm^2 in the two-layer region denoted by a black dot in Fig. 2c.

Next, we correlated the pressure-induced interlayer AF–FM transition with the crystal structure by performing polarized Raman spectroscopy similar to that on the bulk crystals (Fig. 1b,c). As the Raman efficiency decreases rapidly with sample thickness, we focused only on the five-layer region (the green dot in Fig. 2c). Figure 3 shows the polarization-angle dependence of the Raman mode near 107 cm^{-1} in the crossed-polarization configuration (Supplementary Section 1 gives more Raman data). Before applying pressure, the Raman response shows a clear fourfold pattern with a maximum peak shift of about 1.5 cm^{-1} at 300 K (Fig. 3a). This is consistent with the monoclinic structure observed in bulk crystals at high temperatures. However, in contrast to the bulk case, the fourfold pattern persisted on cooling to 10 K (90 K in Fig. 3c) and the rhombohedral phase was not observed. This observation is consistent with a recent Raman study of CrCl$_3$ of 17 nm in thickness[27] and a second harmonic generation study of few-layer CrI$_3$ (ref. [24]). Atomically thin crystals exfoliated at room temperature are

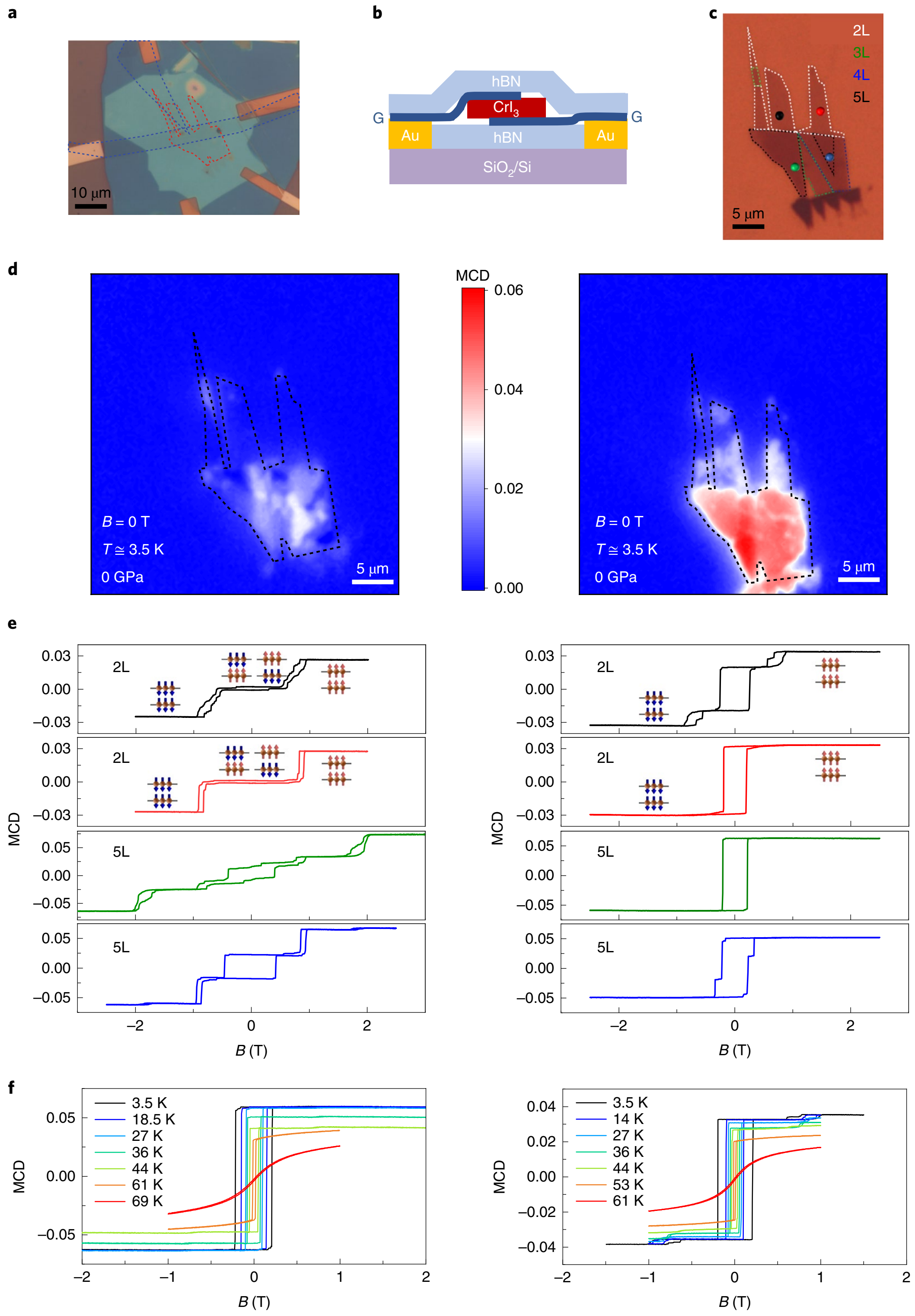

Fig. 2 | Pressure-induced interlayer AF–FM transition in atomically thin CrI$_3$. **a**, Optical micrograph of a tunnel junction employed in this study. The red and blue dashed lines identify the boundaries of CrI$_3$ and few-layer graphene electrodes, respectively. The tunnelling region consists of only the overlapped area of the two electrodes. The device is encapsulated by hBN on both sides (the light and dark blue areas). The rectangular bars are gold electrodes. **b**, Schematic side view of the tunnel junction. Atomically thin CrI$_3$ serves as a tunnel barrier and few-layer graphene (G) (connected to Au contacts) is used as tunnel electrodes. **c**, Optical micrograph of the CrI$_3$ barrier before being integrated into the tunnel junction. The flake has regions of different layer thicknesses identified by dashed lines of different colours. The dots indicate the locations where the MCD data in **e** are acquired. **d**, MCD image of the CrI$_3$ flake before (left) and after (right) applying a pressure of 1.8 GPa. The data were recorded at 3.5 K under zero magnetic field. Scale bars, 10 μm (**a**), 5 μm (**c** and **d**). **e**, Magnetic field dependence of MCD at 3.5 K for two 2-layer (2L) and two 5-layer (5L) regions before (left) and after (right) applying pressure. The colours of the lines match those of the dots identified in **c**. Insets: the spin alignments in the bilayer regions. **f**, MCD versus field at varying temperatures for 5L (left) and 2L (right) regions reveals that the pressure-induced ferromagnetism persists to ~60 K.

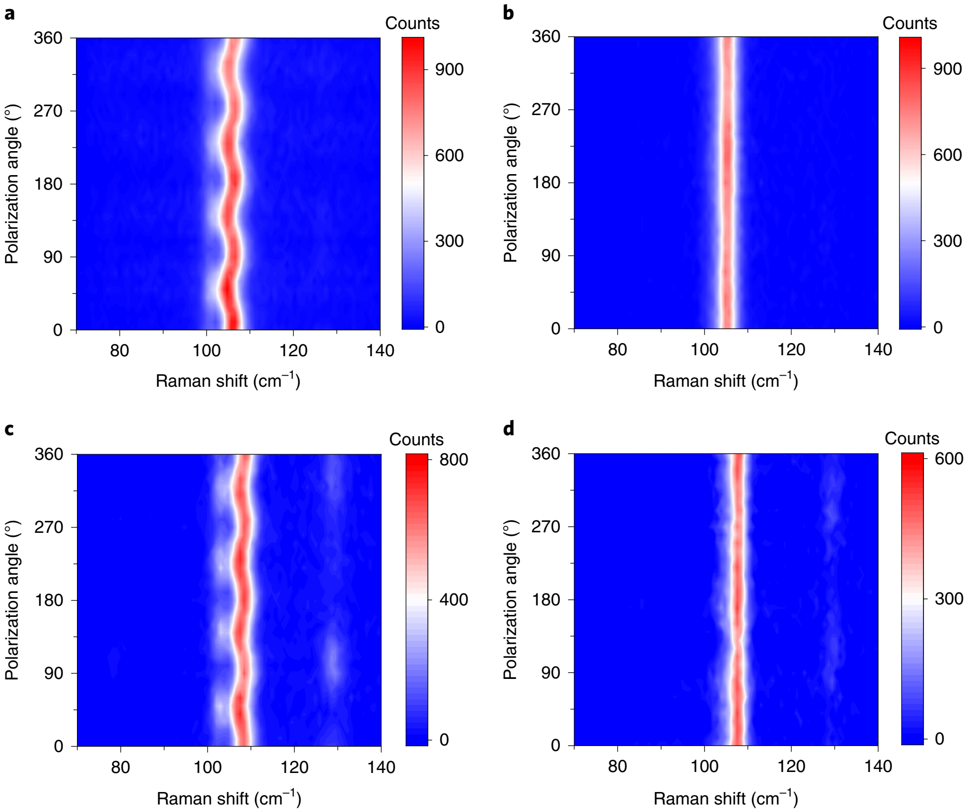

Fig. 3 | Pressure-induced structural phase transition in atomically thin CrI$_3$. a–d, Polarization angle dependence of the Raman spectrum in the crossed-polarization configuration for a five-layer CrI$_3$ sample before (**a** and **c**) and after (**b** and **d**) applying a pressure of 1.8 GPa at 300 K (**a** and **b**) and 90 K (**c** and **d**). The change from a fourfold dependence to no dependence on the polarization angle for the peak energy of the mode at around 107 cm^{-1} is indicative of a monoclinic-to-rhombohedral phase change. No structural phase change was observed on cooling in the absence of pressure regardless of the initial structural phase.

probably kinetically trapped in the monoclinic phase at low temperatures by the encapsulation layers (graphene or hBN). This is possible because the energy difference between the two stacking polytypes is small[3–8]. After applying pressure (Fig. 3b,d), the Raman response changed to that for the rhombohedral structure: no polarization dependence was observed for the peak energy within an uncertainty of 0.2–0.3 cm^{-1}. The dependence was identical at 90 and 300 K, which again supports that the stacking order is locked in encapsulated atomically thin films. Our result, therefore, shows that there is a pressure-induced monoclinic-to-rhombohedral stacking-order change in exfoliated thin CrI$_3$ films, and interlayer AF (FM) coupling is preferred in the monoclinic (rhombohedral) phase. This correlation between the interlayer magnetic ground state and the stacking order agrees with recent ab initio calculations[3–8].

We investigated more than ten samples, several of which consisted of regions of different thicknesses. The effect of pressure and cooling on the magnetic state of these samples is summarized in Supplementary Table 1. We found that, in general, a minimum pressure of 1.7 GPa with cooling is required to achieve a relatively thorough phase transition in bilayer CrI$_3$ and the requirements become less stringent for thicker films. Such a result can be understood from a simple energy consideration. From the bulk data, we obtained that at a low temperature the rhombohedral phase has a lower energy than the monoclinic phase, $F_{R\bar{3}} - F_{C2/m} < 0$. However, a structural phase transition in atomically thin samples on cooling is prevented by an energy barrier imposed by the capping layers and/or substrates. The application of pressure P can facilitate such a structural phase transition by further increasing the energy difference, $P\left(V_{R\bar{3}} - V_{C2/m}\right) < 0$, as the rhombohedral structure has a smaller volume V. The transition is not reversible. In addition, spatial variations in pressure due to the device geometry could contribute to the observed inhomogeneous pressure-induced effect and broad ranges of applied pressure for the structural transition.

Finally, we performed tunnelling measurements on 2D CrI$_3$ junctions to study the pressure effect on magnetism in situ. Figure 4a shows the magnetic field dependence of the tunnel conductance G of the middle two-layer flake (Fig. 2a,c) as a function of pressure in a sequence from top to bottom. Before applying pressure, G shows a jump at the spin-flip transition field $B_{sf} \approx 0.75$ T. This is the spin-filtering effect recently reported in few-layer CrI$_3$ (ref. [8,18–21]). The electron tunnelling rate is higher when the electron spin is aligned with the magnetization of each CrI$_3$ layer. The spin-filtering efficiency can be characterized by the tunnel magnetoresistance (the normalized conductance difference above and below B_{sf} by conductance below B_{sf}). Again, hysteresis is clearly visible. The monotonic decrease of G with increasing field is the response of the graphene electrodes. At 1 GPa, we observed three major changes: the spin-filtering efficiency decreased, B_{sf} shifted to a higher value and the overall G increased. With a further increase of pressure to 1.8 GPa, the spin-filtering effect nearly disappeared. After removing pressure, the behaviour of the junction did not revert back to that before applying pressure. A similar trend was observed in a four-layer tunnel junction under 0–1.4 GPa (Fig. 4b; Supplementary Section 2 gives results from additional devices). There is a second B_{sf} that corresponds to spin flip in the interior layers of CrI$_3$. Both transitions behave similarly as a function of pressure. After removing the pressure, in this device the spin-filtering effect was still clear: the efficiency reduced, but the B_{sf} values reverted back to the values

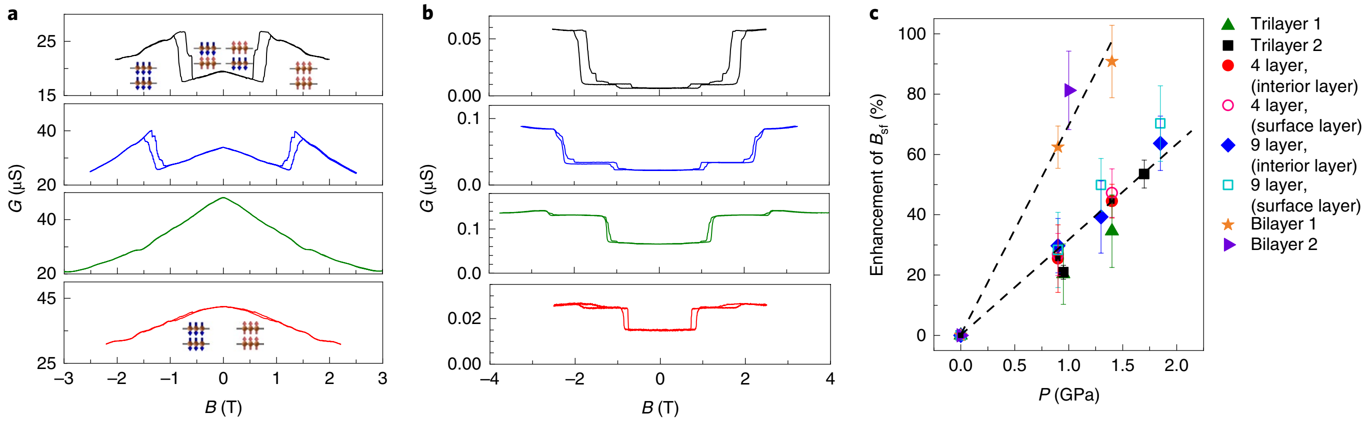

Fig. 4 | Spin-filtering effect in atomically thin CrI3 as a function of pressure. a,**b**, Tunnel conductance *G* versus applied magnetic field *B* of a bilayer CrI_3 tunnel junction at 1.7 K under varying pressure in the order of 0, 1, 1.8 and 0 GPa (from top to bottom). The insets indicate the spin alignments. **b**, Same measurement of a four-layer CrI_3 tunnel junction under varying pressure in the order of 0, 0.9, 1.4 and 0 GPa (from top to bottom). The bias voltage for all the measurements was 10 mV. **c**, Enhancement of the spin-flip transition field $\frac{B_{sf}(P)-B_{sf}(0)}{B_{sf}(0)}$ as a function of pressure *P* from six different devices. The dashed straight lines are a guide to the eye. The spin-flip transition field for each magnetic field sweep direction was estimated from the field that corresponded to the steepest change of *G*. The error bars were estimated from the width of the rise/fall of *G* with field in the transition region. B_{sf} in **c** was calculated as the average for the two sweep directions.

before applying pressure. We summarize the pressure dependence of B_{sf} in the form of relative enhancement over the zero pressure value in Fig. 4c. The dependence increased monotonically with pressure for samples of different thicknesses. The rate was roughly the same for all the samples except that for the bilayers, which was about twice as large.

The spin-filtering efficiency is determined by the fraction of the AF area in the junction. The significantly suppressed spin-filtering effect under high pressure (1.8 GPa) in the bilayer sample is consistent with a nearly complete structural phase transition. The residual effect under intermediate pressure (0.9–1.4 GPa) in the four-layer sample can be attributed to a spatially mixed AF and FM phase in CrI_3. On the other hand, spin flip occurs when the Zeeman splitting energy is comparable to the interlayer AF exchange energy $J_\perp \approx g\mu_B m_S B_{sf}$, where $g \approx 2$ is the electron *g* factor, μ_B is the Bohr magneton and $m_S \approx \frac{3}{2}$ is the spin magnetic quantum number of the Cr^{3+} cations[25]. In bilayer CrI_3, $J_\perp$ is about 0.25 meV with $B_{sf} \approx 0.75$ T under zero pressure, and it nearly doubles under 1.5 GPa. Our first-principles calculations show that for bilayer CrI_3 in space group *C*2/*m*, $J_\perp$ remains AF, and its magnitude increases nearly linearly with decreasing layer separation by a few percent (Supplementary Section 4). The result shown in Fig. 4c is thus consistent with the picture of layer compression without a stacking-order change on the application of pressure. The reduction in layer separation also contributes to the observed increase of the overall conductance. However, future theoretical studies are needed for a more quantitative comparison between experiment and theory and to understand the unusually large pressure effect on the interlayer exchange interaction in bilayer CrI_3.

In conclusion, we experimentally demonstrated control of the interlayer magnetic ground state through the crystal stacking order in atomically thin van der Waals magnets by the application of hydrostatic pressure. Pressure can also be employed to strengthen the interlayer exchange interaction. The established stacking-dependent magnetic order suggests the possibility of engineering periodic variations in the interlayer exchange energy by forming moiré superlattices in twisted bilayers[30]. Our findings, therefore, not only shed light on the physical origin of the thickness-dependent magnetic ground state in atomically thin CrI_3, but also pave the path for engineering moiré magnetism in van der Waals magnets[3,9].

Online content

Any methods, additional references, Nature Research reporting summaries, source data, statements of code and data availability and associated accession codes are available at https://doi.org/10.1038/s41563-019-0506-1.

Received: 26 May 2019; Accepted: 11 September 2019;
Published online: 28 October 2019

References

1. Castro Neto, A. H., Guinea, F., Pere, N. M. R., Novoselov, K. S. & Geim, A. K. The electronic properties of graphene. *Rev. Mod. Phys.* **81**, 109–162 (2009).
2. Cao, H. B. et al. Low-temperature crystal and magnetic structure of α-$RuCl_3$. *Phys. Rev. B* **93**, 134423 (2016).
3. Sivadas, N., Okamoto, S., Xu, X., Fennie, C. J. & Xiao, D. Stacking-dependent magnetism in bilayer CrI_3. *Nano Lett.* **18**, 7658–7664 (2018).
4. Jiang, P. et al. Stacking tunable interlayer magnetism in bilayer CrI_3. *Phys. Rev. B* **99**, 144401 (2019).
5. Soriano, D., Cardoso, C. & Fernández-Rossier, J. Interplay between interlayer exchange and stacking in CrI_3 bilayers. *Solid State Commun.* **299**, 113662 (2019).
6. Jang, S. W., Jeong, M. Y., Yoon, H., Ryee, S. & Han, M. J. Microscopic understanding of magnetic interactions in bilayer CrI_3. *Phys. Rev. Mater.* **3**, 031001 (2019).
7. Lei, C. et al. Magnetoelectric response of antiferromagnetic van der Waals bilayers. Preprint at https://arxiv.org/abs/1902.06418 (2019).
8. Wang, Z. et al. Very large tunneling magnetoresistance in layered magnetic semiconductor CrI_3. *Nat. Commun.* **9**, 2516 (2018).
9. Tong, Q., Liu, F., Xiao, J. & Yao, W. Skyrmions in the moiré of van der Waals 2D magnets. *Nano Lett.* **18**, 7194–7199 (2018).
10. Burch, K. S., Mandrus, D. & Park, J. G. Magnetism in two-dimensional van der Waals materials. *Nature* **563**, 47–52 (2018).
11. Gong, C. & Zhang, X. Two-dimensional magnetic crystals and emergent heterostructure devices. *Science* **363**, eaav4450 (2019).
12. Gibertini, M., Koperski, M., Morpurgo, A. F. & Novoselov, K. S. Magnetic 2D materials and heterostructures. *Nat. Nanotechnol.* **14**, 408–419 (2019).
13. Gong, C. et al. Discovery of intrinsic ferromagnetism in two-dimensional van der Waals crystals. *Nature* **546**, 265–269 (2017).
14. Huang, B. et al. Layer-dependent ferromagnetism in a van der Waals crystal down to the monolayer limit. *Nature* **546**, 270–273 (2017).
15. Jiang, S., Shan, J. & Mak, K. F. Electric-field switching of two-dimensional van der Waals magnets. *Nat. Mater.* **17**, 406–410 (2018).
16. Huang, B. et al. Electrical control of 2D magnetism in bilayer CrI_3. *Nat. Nanotechnol.* **13**, 544–548 (2018).
17. Jiang, S., Li, L., Wang, Z., Mak, K. F. & Shan, J. Controlling magnetism in 2D CrI_3 by electrostatic doping. *Nat. Nanotechnol.* **13**, 549–553 (2018).

18. Song, T. et al. Giant tunneling magnetoresistance in spin-filter van der Waals heterostructures. *Science* **360**, 1214–1218 (2018).
19. Klein, D. R. et al. Probing magnetism in 2D van der Waals crystalline insulators via electron tunneling. *Science* **360**, 1218–1222 (2018).
20. Kim, H. H. et al. One million percent tunnel magnetoresistance in a magnetic van der Waals heterostructure. *Nano Lett.* **18**, 4885–4890 (2018).
21. Song, T. et al. Voltage control of a van der Waals spin-filter magnetic tunnel junction. *Nano Lett.* **19**, 915–920 (2019).
22. Jiang, S., Li, L., Wang, Z., Mak, K. F. & Shan, J. Spin transistor built on 2D van der Waals heterostructures. *Nat. Electron.* **2**, 159–163 (2019).
23. Thiel, L. et al. Probing magnetism in 2D materials at the nanoscale with single-spin microscopy. *Science* **364**, 973–976 (2019).
24. Sun, Z. et al. Giant and nonreciprocal second harmonic generation from layered antiferromagnetism in bilayer. *Nature* **572**, 497–501 (2019).
25. McGuire, M. A., Dixit, H., Cooper, V. R. & Sales, B. C. Coupling of crystal structure and magnetism in the layered ferromagnetic insulator CrI_3. *Chem. Mater.* **27**, 612–620 (2015).
26. Djurdjić-Mijin, S. et al. Lattice dynamics and phase transition in CrI_3 single crystals. *Phys. Rev. B* **98**, 104307 (2018).
27. Klein, D. R. et al. Giant enhancement of interlayer exchange in an ultrathin 2D magnet. Preprint at https://arxiv.org/abs/1903.00002 (2019).
28. Larson, D. T. & Kaxiras, E. Raman spectrum of CrI_3: an ab initio study. *Phys. Rev. B* **98**, 085406 (2018).
29. Song, T. et al. Switching 2D magnetic states via pressure tuning of layer stacking. Preprint at https://arxiv.org/abs/1905.10860 (2019).
30. Jung, J., Raoux, A., Qiao, Z. & MacDonald, A. H. Ab initio theory of moiré superlattice bands in layered two-dimensional materials. *Phys. Rev. B* **89**, 205414 (2014).

Acknowledgements

We thank D. Graf and K. Huang for fruitful discussions on high-pressure cell operation, and G. H. Olsen and Z. He on density functional theory calculations. This work was supported by the US Army Research Office (ARO) under award W911NF-17-1-0605 (high-pressure cell set-up), the Office of Naval Research (ONR) under award N00014-18-1-2368 (device fabrication) and the Center for Emergent Materials, an NSF MRSEC under award number DMR-1420451 (bulk CrI_3 crystal growth and optical measurements). This work was also partially supported by the Cornell Center for Materials Research with funding from the NSF MRSEC program under DMR-1719875 (first principles calculations and transport measurements). The growth of hBN crystals was supported by the Elemental Strategy Initiative conducted by the MEXT, Japan, and the CREST(JPMJCR15F3), JST. D.W. gratefully acknowledges the financial support by the German Science Foundation (Deutsche Forschungsgemeinschaft, DFG) under the fellowship number WE6480/1. K.F.M. acknowledges support from a David and Lucille Packard Fellowship and a Sloan Fellowship.

Author contributions

T.L., S.J., K.F.M. and J.S. designed the study. T.L. developed the high-pressure cell set-up. T.L. and S.J. fabricated the devices and performed the measurements with the assistance of Z.W. and Y.X. N.S. and C.J.F. performed the first principles calculations. D.W. and J.E.G. grew the bulk CrI_3 crystals and K.W. and T.T. grew the bulk hBN crystals. T.L., K.F.M. and J.S. co-wrote the manuscript. All the authors discussed the results and commented on the manuscript.

Competing interests

The authors declare no competing interests.

Additional information

Supplementary information is available for this paper at https://doi.org/10.1038/s41563-019-0506-1.

Correspondence and requests for materials should be addressed to K.F. or J.S.

Methods

Growth of CrI_3 bulk crystals. Bulk CrI_3 crystals were synthesized by chemical vapour transport, as described previously[31]. The elements were sealed in an evacuated ampoule (109.0 mg Cr chunks, 1 equiv., 99.999% purity (Alfa Aesar); 798.0 mg I_2 crystals, 1.5 equiv., 99.999% purity (Alfa Aesar)). The ampoule was heated to 650 °C at the feed and 550 °C at the growth zone. After a week, the ampoule was cooled and the reaction yielded crystals of 1–2 mm edge length. CrI_3 produced by this method crystallized in the $C2/m$ space group with typical lattice parameters of $a = 6.904$ Å, $b = 11.899$ Å, $c = 7.008$ Å and $\beta = 108.74°$ at room temperature. In a typical sample, the crystals exhibited a Curie temperature of 61 K as well as a structural phase transition to the space group $R\bar{3}$ at 210–220 K (ref. [25]).

Device fabrication. CrI_3 tunnel junctions were fabricated by the layer-by-layer dry-transfer method[32]. Atomically thin flakes of hBN, graphite and CrI_3 were mechanically exfoliated from bulk crystals onto silicon substrates covered by a 300 nm thermal oxide layer. The flakes were picked up in sequence by a stamp made of a thin film of polycarbonate on polydimethylsiloxane. The entire stack was then released onto a substrate with prepatterned titanium/gold (Ti/Au 5 nm/35 nm) electrodes. The residual polycarbonate on the device surface was dissolved in chloroform before the measurements. Both the exfoliation and the transfer processes were performed in a nitrogen-filled glove box to avoid the degradation of CrI_3. The thickness of atomically thin CrI_3 samples was initially estimated from their optical reflection contrast, and later verified by MCD or atomic force microscopy measurements.

High-pressure experiments. Hydrostatic pressure has emerged as a powerful method to tune the properties of layered materials[33–35]. A piston high-pressure cell compatible with electrical transport measurements at low temperature (easyCell 30, Almax easyLab) was employed. The cylindrical cell has an inner bore diameter of about 3.9 mm. Hydrostatic pressure was applied on the samples through pressure transmission medium, a pentane and isopentane mixture (1:1), which freezes around 160 K. The typical range of pressure that can be accessed at low temperature is 1–2 GPa. Supplementary Section 5 gives details on mounting the devices in the pressure cell.

Pressure was applied (or changed) at room temperature. The cell was then cooled to low temperature for the measurements. Two types of manometers were used for the pressure calibration. At room temperature, the pressure was calibrated by measuring the resistance of a manganin wire (~10 cm long) wound into a coil[36]. At low temperature, the pressure was calibrated by measuring the superconducting transition temperature of a tin wire[36]. The pressure was generally about 0.1–0.3 GPa lower at the low temperature than at room temperature due to the freezing of the pressure transmission medium.

MCD microscopy. MCD measurements were performed in an attoDry1000 cryostat with a base temperature of 3.5 K. For non-imaging measurements, a HeNe laser at 633 nm was used. The laser beam was coupled into and out of the cryostat using free-space optics. It was focused onto the sample by a cold objective. The beam size on the sample was about 1 μm², and the power no more than 10 μW. The incident beam was modulated between left and right circular polarization by a photoelastic modulator at 50.1 kHz. The reflected beam was collected by the same objective and detected by a photodiode. The MCD signal was determined as a ratio of the a.c. component at 50.1 kHz (measured by a lock-in amplifier) and the d.c. component (measured by a digital multimeter) of the reflected light intensity.

In MCD imaging, a broad-field illumination and a nitrogen-cooled CCD (charge-coupled device) were used. The light source was selected from an incoherent white light using a bandpass filter centred at 632 nm. A linear polarizer and a quarter-wave plate were used to generate circularly polarized light. The MCD image was calculated as the normalized difference between the left and right circularly polarized light reflection by the total reflection. The spatial resolution was diffraction limited (~500 nm).

Polarized Raman spectroscopy. Raman spectroscopy was performed using a homebuilt microscope in the back-scattering geometry. A solid-state laser at 532 nm was employed as the excitation source. The laser beam was focused onto the CrI_3 samples along the c axis by a ×40 objective. The scattered light was collected by the same objective and detected by a spectrometer with a 1,800 grooves mm^{-1} diffraction grating and a nitrogen-cooled CCD. The polarized Raman modality was used to characterize the crystal structure, as demonstrated in recent studies of 2D van der Waals materials[37–39]. To this end, the laser beam was passed through a linear polarizer and a half-wave plate. The latter varies the polarization angle in the crystal a–b plane. The scattered light passed through the same half-wave plate and a second linear polarizer, which selects the component either parallel or perpendicular to the incident beam polarization (referred to as the parallel- and crossed-polarization configuration, respectively).

The polarized Raman spectroscopy in crystals of both the $R\bar{3}$ and $C2/m$ groups was analysed previously[26]. In particular, for the doubly degenerate ^1E_g and ^2E_g modes (in the rhombohedral phase) and the non-degenerate A_g and B_g modes (in the monoclinic phase) that have been examined in this study, the Raman tensors are derived as:

$$^1E_g = \begin{pmatrix} c & d & e \\ d & -c & f \\ e & f & 0 \end{pmatrix},\ ^2E_g = \begin{pmatrix} d & -c & -f \\ -c & -d & e \\ -f & e & 0 \end{pmatrix},\ A_g = \begin{pmatrix} a & 0 & d \\ 0 & c & 0 \\ d & 0 & b \end{pmatrix},$$

$$B_g = \begin{pmatrix} 0 & e & 0 \\ e & 0 & f \\ 0 & f & 0 \end{pmatrix}$$

In the crossed-polarization configuration, the Raman intensity for the two E_g modes is given as $I = (^1E_g)_{\mathrm{cross}}|c\sin(2\theta) - d\cos(2\theta)|^2$ and $I = (^2E_g)_{\mathrm{cross}}|c\cos(2\theta) + d\sin(2\theta)|^2$, where θ is the polarization angle with respect to the a axis. The total intensity of the two degenerate modes ($c^2 + d^2$) is polarization independent. A similar result can be derived for the parallel-polarization configuration.

The result is different for the non-degenerate A_g and B_g modes in the monoclinic phase. The Raman intensity of each mode shows a fourfold polarization dependence, $I = (A_g)_{\mathrm{cross}} = a^2\sin^2(2\theta)$, $I = (B_g)_{\mathrm{cross}} = e^2 cos^2(2\theta)$, but they are off by π/4. Here we assumed $a \approx -c$, because the symmetry of $A_g + B_g$ should match the symmetry of $^1E_g + {}^2E_g$ (ref. [27]). The total intensity of these two spectrally unresolved modes shows a four-fold polarization dependence for the peak energy. Similar result can be derived for the parallel-polarization configuration.

Data availability

The data supporting the plots within this paper and other findings of this study are available from the corresponding authors upon request.

References

31. Shcherbakov, D. et al. Raman spectroscopy, photocatalytic degradation, and stabilization of atomically thin chromium tri-iodide. *Nano Lett.* **18**, 4214–4219 (2018).
32. Wang, L. et al. One-dimensional electrical contact to a two-dimensional material. *Science* **342**, 614–617 (2013).
33. Yankowitz, M. et al. Dynamic band-structure tuning of graphene moiré superlattices with pressure. *Nature* **557**, 404–408 (2018).
34. Yankowitz, M. et al. Tuning superconductivity in twisted bilayer graphene. *Science* **363**, 1059–1064 (2019).
35. Kim, J. S. et al. Towards band structure and band offset engineering of monolayer $Mo_{(1-x)}W_{(x)}S_2$ via Strain. *2D Mater.* **5**, 015008 (2018).
36. Eremets, M. *High Pressure Experimental Methods* (Oxford Univ.ersity Press, Oxford, 1996).
37. Tian, Y., Gray, M. J., Ji, H., Cava, R. J. & Burch, K. S. Magneto-elastic coupling in a potential ferromagnetic 2D atomic crystal. *2D Mater.* **3**, 025035 (2016).
38. Kim, K. et al. Suppression of magnetic ordering in XXZ-type antiferromagnetic monolayer $NiPS_3$. *Nat. Commun.* **10**, 345 (2019).
39. Du, L. et al. 2D proximate quantum spin liquid state in atomic-thin α-$RuCl_3$. *2D Mater.* **6**, 015014 (2018).